Journal of Magnetic Resonance **141,** 217–227 (1999)
Article ID jmre.1999.1904, available online at http://www.idealibrary.com on IDEAL®

A System for Low Field Imaging of Laser-Polarized Noble Gas

G. P. Wong,* C. H. Tseng,*,† V. R. Pomeroy,‡ R. W. Mair,* D. P. Hinton,§ D. Hoffmann,* R. E. Stoner,* F. W. Hersman,‡ D. G. Cory,† and R. L. Walsworth*

**Harvard-Smithsonian Center for Astrophysics, Cambridge, Massachusetts 02138; †Department of Nuclear Engineering, MIT, Cambridge, Massachusetts 02138; ‡Department of Physics, University of New Hampshire, Durham, New Hampshire 03824; and §Massachusetts General Hospital, NMR Center, Charlestown, Massachusetts 02129*

Received February 4, 1999; revised August 10, 1999

We describe a device for performing MRI with laser-polarized noble gas at low magnetic fields (<50 G). The system is robust, portable, inexpensive, and provides gas-phase imaging resolution comparable to that of high field clinical instruments. At 20.6 G, we have imaged laser-polarized ^{3}He (Larmor frequency of 67 kHz) in both sealed glass cells and excised rat lungs, using ~0.1 G/cm gradients to achieve ~1 mm^2 resolution. In addition, we measured ^{3}He T_2^* times greater than 100 ms in excised rat lungs, which is roughly 20 times longer than typical values observed at high (~2 T) fields. We include a discussion of the practical considerations for working at low magnetic fields and conclude with evidence of radiation damping in this system.

Key Words: **laser-polarized noble gas; low magnetic field; magnetic resonance imaging; lung imaging; radiation damping.**

INTRODUCTION

Recently, laser-polarized (LP) spin-$\frac{1}{2}$ noble gases (^{3}He and ^{129}Xe) have been the focus of intense interest in the magnetic resonance community. Starting with LP ^{129}Xe gas imaging of excised mouse lungs in 1994 by Albert *et al.* (*1*), there have been numerous advances made with LP ^{129}Xe and ^{3}He imaging. Notable examples include live animal and human lung imaging (*2*), as well as imaging and time-dependent diffusion studies of materials (*3, 4*). The interest in LP noble gases arises from the large nuclear spin polarization (>10%) provided by laser-polarization techniques (*5, 6*). Whereas the spin polarization of conventional, thermally polarized systems is a linear function of the applied magnetic field, the spin polarization of LP noble gas is determined by factors that are *not* dependent on the applied magnetic field, such as laser power and gas mixtures. Consequently, it is possible to perform sensitive NMR and MRI on LP noble gases at substantially lower field strengths. For example, Darrasse *et al.* recently demonstrated LP ^{3}He human lung imaging at 1000 G (0.1 T) (*7*), while Saam and coworkers obtained one dimensional profiles of cells filled with LP ^{3}He at 31 G (*8*). In addition, using superconducting quantum interference devices (SQUIDs), Augustine *et al.* imaged LP ^{3}He gas and ^{129}Xe solid at liquid helium temperature (4 K) and 5.4 G (*9*).

There are important advantages to low field MRI of LP noble gas because certain fundamental imaging constraints are diminished. In particular, distortions and line broadening that result from large background gradients produced by magnetic susceptibility differences in heterogeneous samples are greatly reduced. Also, low Larmor frequencies (~kHz) correspond to greater electromagnetic field skin depths. Consequently, RF pulses can penetrate thin metallic shielding and thus allow gas-phase imaging inside conductors. In addition, a low field system is simple, inexpensive, portable, and easy to maintain. Magnetic field requirements are easily met with a low-power, wire-wound solenoid capable of producing absolute field homogeneity comparable to, if not better than, typical high field clinical magnets. Also, the small external field and low (kHz) RF frequencies do not necessitate site restrictions, such as large shielded rooms, thus permitting operation in restricted environments (e.g., a space station) and with subjects and systems incompatible with high magnetic fields or high RF frequencies (e.g., patients with sensitive implants or experimental apparatus with integrated electronics).

Recently, we demonstrated fast, single-scan 2D imaging at 20.6 G of LP ^{3}He in sealed glass phantoms (for an example, see Fig. 1) (*10*). In this report, we describe the low field imaging system used in those experiments, present recent experimental results (e.g., low field MRI of LP ^{3}He imbibed in excised rat lungs), and discuss advantages and practical considerations of imaging at low fields. We also present measurements of radiation damping in LP ^{3}He at low field and conclude with a discussion of this effect on our experiments.

SYSTEM OVERVIEW

The Magnet

We built a wire-wound solenoid using a design by Hanson and Pipkin (*11*). It is capable of producing a magnetic field of up to 100 G without significant resistive heating and consists of four layers of 19-gauge copper wire wrapped around a 114-cm long, 30-cm o.d. aluminum cylinder. Two HP6200B DC power supplies provide the current required to power the magnet—

1090-7807/99 $30.00

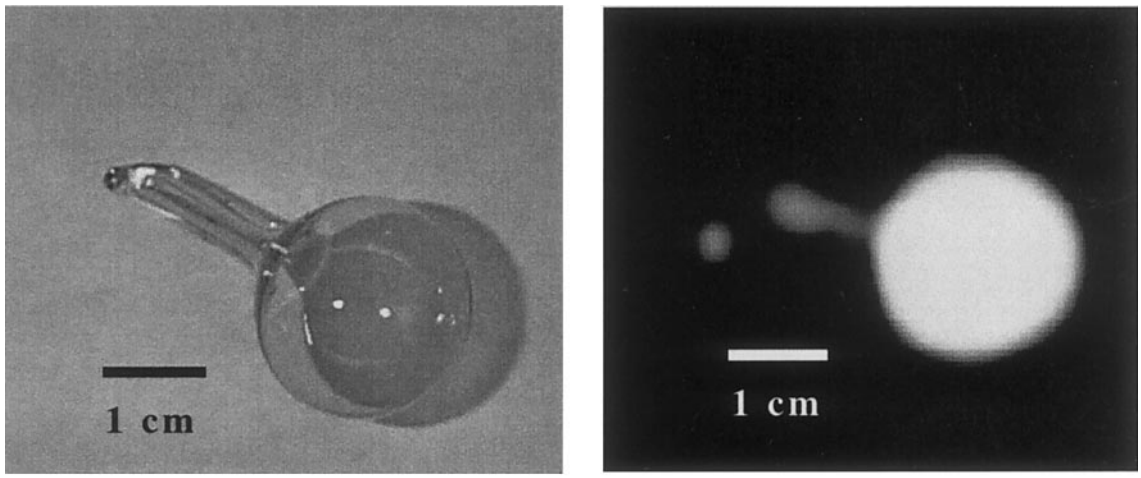

FIG. 1. Example ^{3}He test phantom and low field image. (a) Photograph of a sealed glass cell filled (at STP) with 2.7 atm ^{3}He, 100 Torr N_2, and Rb metal. Prior to filling, the cell was baked at high temperature under vacuum for 6 days; (b) Laser-polarized ^{3}He MRI of the test phantom at 20.6 G using a gradient echo FLASH sequence. Note that the small volume pull-off stem of the cell is visible to the left; the protrusion to the lower left of the pull-off is the zero-frequency artifact, and the discrepancy in the stem length is due to image foreshortening.

typically, 0.4 amps to each of the four winding layers to establish an applied field of ~20 G.

As Hanson and Pipkin showed, the magnetic field homogeneity in the central region of a solenoid can be characterized by the field along the axis (taken as the z direction) and its derivatives. This axial field $B_z(z, r = 0)$ is primarily determined by the solenoid dimensions, and given the solenoid radius a and the angle θ (which is defined by the symmetry axis and the line joining the solenoid center to the radius at the bore end), can be written as

$$B_z(z, 0) = \frac{4\pi NI}{10}\cos(\theta)\left[1 - \frac{3}{2}\sin^4(\theta)\left(\frac{z}{a}\right)^2 - \frac{5}{8}\sin^6(\theta)(7\cos^2(\theta) - 3)\left(\frac{z}{a}\right)^4 - \cdots\right]. \quad [1]$$

Here, I is the applied current and N is the number of turns per unit length. We also included second- and fourth-order correction coils wound on the outside of the main solenoid. The angle θ_2, defined by the dimensions of the second-order correction coil in analogy with θ is chosen so that the fourth-order term in Eq. [1] equals zero (i.e., $7\cos^2(\theta_2) - 3 = 0$). The fourth-order correction coil is a split solenoid and may be analyzed as two different solenoids with opposing currents and characteristic angles θ_4' and θ_4. The angles are chosen so that the second-order term in Eq. [1] goes to zero (i.e., $\cos(\theta_4')\sin^4(\theta_4') - \cos(\theta_4)\sin^4(\theta_4) = 0$). For convenience, we follow Hanson and Pipkin's example and choose $\theta_4' = \theta_2$.

A simple coil loop of n turns with applied current I is used to shim the linear component of $B_z(z, 0)$; its field is described by

$$B_z^{(1)}(z, 0) = \frac{2\pi nI}{10}\frac{\sin^3(\theta)}{a}\left[1 + 3\cos(\theta)\sin(\theta)\left(\frac{z}{a}\right) + \frac{3}{2}\sin^2(\theta)(5\cos^2(\theta) - 1)\left(\frac{z}{a}\right)^2 + \cdots\right]. \quad [2]$$

This linear correction coil is offset so that the second order term of $B_z^{(1)}$ is zero at the center of the main solenoid (i.e., $5\cos^2(\theta_1) - 1 = 0$, where θ_1 is defined by the position of the linear coil).

The magnet's field homogeneity was determined by measuring free induction decays (FIDs) of LP ^{3}He sealed in a spherical 8.5 cc test cell placed at the solenoid's center. At main fields of ~20 G, typical linewidths of 2–3 Hz were observed, with even narrower linewidths (<1 Hz) under ideal conditions. Such ^{3}He linewidths were suitable for the imaging experiments performed; higher homogeneity would require magnetic shielding from the background field of ~1 G and shim coils to compensate for radial gradients of B_z (the existing coils correct for axial gradients only).

Figure 2 shows an example of the measured temporal stability of the field during the first 12 h after the magnet was turned on. There is an initial large drift in the field (~0.1%) as the DC current supplies and detection electronics warm up. After about an hour, the field equilibrates, providing short-term

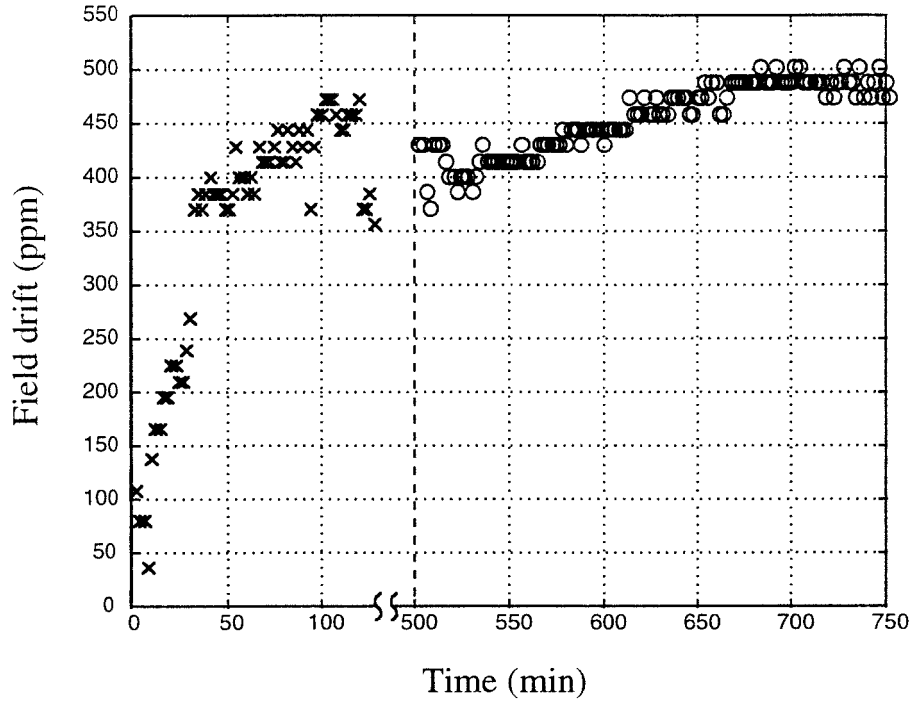

FIG. 2. Typical temporal stability of solenoid's magnetic field (~20 G) without stabilization. Two data sets are shown. The first (×) is taken just after turning on the magnet; the large initial drift is due to system warm up. The second data set (○) is taken much later, after the current supplies and electronics have stabilized.

stability (on minute time scales) of a few parts in 10^5; with imaging times less than 30 s, this stability is sufficient. Straightforward modifications such as shielding, active feedback control of the solenoid current, and temperature control of the magnet would increase both the magnetic field stability and homogeneity.

Electronics

The RF source is an unamplified Wavetek DDS function generator Model 29. This device provides a frequency reference for a lockin amplifier (Stanford Research Systems, Inc., Model SR830), while its main output is gated by a TTL pulse (whose duration sets the RF pulse width) and drives a set of Helmholtz coils surrounding the sample. A pair of orthogonally mounted pickup coils around the sample sense the NMR signal, which is amplified and filtered by a low noise preamplifier (Stanford Research Systems, Inc., Model SR560). After this stage, the lock-in amplifier further amplifies and filters the NMR signal components near the reference frequency.

The two drive coils surrounding the sample each consist of six turns of no. 25 HAPT wire wound around a square 7 cm per side. The drive coil pair are separated by 8.5 cm and tuned with external capacitors to the spin Larmor frequency (e.g., 67 kHz for ^{3}He at 20.6 G). The Q of this drive coil configuration is ~10. The pickup coils are mounted orthogonal to the drive coils, and are wired to allow differential signal amplification that rejects common-mode noise (see Fig. 3a). Each pickup coil consists of ~200 turns of no. 32 HAPT wire on a round nylon form 7.5 cm in diameter. The coils are spaced 4.5 cm apart and are tuned to the spin Larmor frequency by external capacitors; the measured Q is approximately 60. The sample holder is a 2.5 × 3.2 × 9 cm long trough nestled between the drive and pickup coils. The whole assembly (coils + sample holder) is rigidly mounted together with one of the drive coils on a hinged lid to allow access into the sample holder. This is shown in Fig. 3b.

Imaging gradients are produced by a homemade set of unshielded Golay coils (for dB_z/dx and dB_z/dy, i.e., G_x and G_y) and a pair of anti-Helmholtz coils (for dB_z/dz, i.e., G_z) wound on a 14-cm diameter G-10 cylinder, following the description found in Callaghan (*12*). With our present amplifiers, the anti-Helmholtz coils (also known as a Maxwell pair) provide a maximum gradient of 380 mG/cm, while the Golay coils produce up to 630 mG/cm. Typically, we used these gradients up to 50% of their full strength for durations of 10 ms. The gradients, as well as the RF trigger pulses, are controlled by a commercial Bruker AMX console. Detected NMR signals are routed directly from the lock-in amplifier outputs into the console's digitizer (thus bypassing the console's normal high frequency receivers and mixers). Figure 4 shows a schematic of the system. One could easily replace the AMX console with a desktop computer equipped with a Digital–Analog Acquisi-

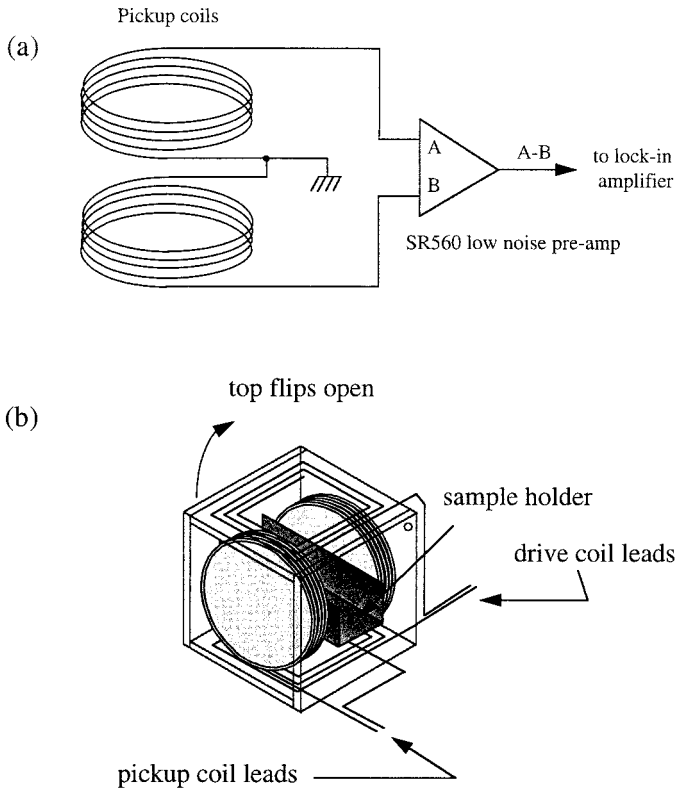

FIG. 3. (a) Configuration used to reject common-mode noise in the pickup coils. (b) Sample holder with orthogonal RF drive (square) and pickup (round) coils. The coil geometry was inspired by our earlier maser and adiabatic fast passage (AFP) LP noble gas experiments (Ref. *25*).

tion (DAQ) board. The DAQ board should have at least two analog outputs for gradient control, a TTL output to trigger and set the duration of the RF pulse, and a sufficiently fast digitizer (~50 kHz).

METHOD

A cell containing a mixture of 3 atm of ^{3}He, ~100 Torr nitrogen and Rb metal was placed in a blown-air oven and heated to 180°C. Optical pumping of the Rb vapor by circularly polarized light from a 15 Watt fiber-coupled laser diode array (Opto Power Corporation, model OPCA-015-FCPS) polarized the ^{3}He via spin-exchange to approximately 10% after 3–4 h (in our small 8.5 cc sealed test cells). For the lung imaging experiments, a valved 65 cc cell was used; after laser-polarization, measured shots of 3 to 5 cc's of ^{3}He gas were forced into the excised rat lungs for imaging.

Excised tissue was obtained from 300–400 g male Sprague–Dawley rats. Both the left and multiple right lobes of the lungs, along with several cm of trachea, were removed postmortem. A 25 gauge butterfly tube (with needle removed) was placed into the trachea and secured with silk suture. Forty-eight inches of high pressure plastic tubing extended down the bore of the low field magnet to connect the lung tissue to a syringe that was filled with LP ^{3}He gas directly from the valved glass polarization cell. Excised lungs were used in the imaging experiments within 3 h of harvest. All animal procedures were approved by the Massachusetts General Hospital Subcommittee on Research Animal Care.

RESULTS

Pulse flip angles and T_1 of the LP gas were measured by recording the FIDs following each of a series of low flip angle (α) pulses. Given a time T_R between each pulse, the jth FID signal amplitude S_j can be expressed as

$$S_j = S_0(\cos\alpha)^{j-1}\exp[-(j-1)\times T_R/T_1]. \qquad [3]$$

Figure 5 shows typical FID and flip angle calibration data taken at 20.6 G for LP ^{3}He sealed in a glass cell. Each point of the flip angle calibration data represents the logarithm of the integrated real part of each successive FID's fourier transform (which is proportional to log $[S_j]$); plotting log$[S_j]$ versus j should be linear with a slope equal to $[\ln(\cos\alpha) - T_R/T_1]$. With $T_R \ll T_1$, one can determine the flip angle α; consequently, once α is known, repeating the experiment with a long T_R allows one to measure T_1.

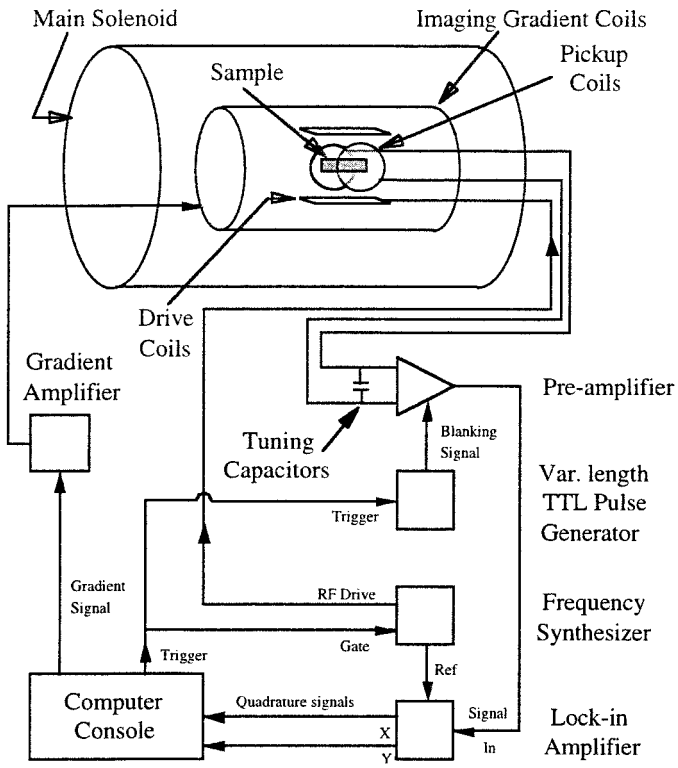

FIG. 4. Schematic of low-field MRI system. A variable length TTL signal blanks the preamplifier slightly longer than the RF pulse to avoid amplifying any coil ring-down.

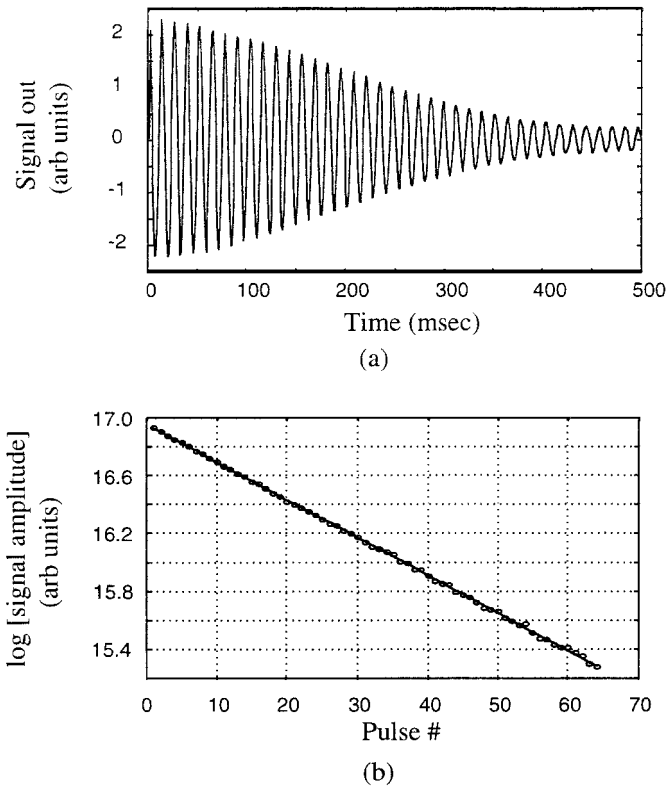

FIG. 5. (a) Typical free-induction decay (FID) observed for LP ^{3}He at 20.6 G and (b) flip angle calibration data obtained using a series of low flip angle pulses on a LP ^{3}He sealed glass phantom; the line shown is a fit to the data. RF pulse width was 2 ms, and the frequency synthesizer was set to output 2.0 V_{pp} at 67.0 kHz. For each FID acquired for (b) (of which (a) was the first), the linewidth was ~2 Hz with initial SNR ~1700. Acquisition of 64 FIDs took ~84 s, which was much less than the T_1 (~100 h) of the cell. Fitting the data to the log of Eq. [3] indicated a flip angle α of 13.0° for this RF pulse.

To demonstrate the efficacy of low field imaging with laser-polarized noble gases for samples of biological interest, we imaged excised rat lungs filled with LP ^{3}He (Fig. 6) using a FLASH imaging sequence: 128 concentric phase encodes steps; 12° flip angle; gradient strength and duration was ~0.1 G/cm, 10 ms; total imaging time was ~25 s. No slice selection was used, and the two-dimensional resolution was ~1 mm^2. In different experimental runs we measured ^{3}He relaxation times T_1 from 16 to 63 s (Fig. 7), which is within the range of values reported at high field due to remnant paramagnetic oxygen in the lung gas space (*13*). We also measured the low-field ^{3}He T_2^* in excised rat lungs to be greater than 100 ms, which is significantly longer than the approximately 5 ms T_2^* observed for LP ^{3}He in guinea pig and human lungs at 2 and 1.5 T, respectively (*14, 2*). This longer ^{3}He T_2^* is a result of the reduced effect of magnetic susceptibility heterogeneity at low magnetic fields, and is one of the advantages of low-field imaging. In addition, there was a consistent trend of increasing T_2^* with subsequent low angle RF pulses (corresponding to decreasing longitudinal LP ^{3}He magnetization), which prompted us to investigate radiation damping in this system. A brief discussion of these measurements is given later in this paper.

DISCUSSION

(i) Dependence of Signal-to-Noise-Ratio on Magnetic Field Strength

In conventional NMR and MRI, nuclear spin polarization P is determined by the temperature T and magnetic field strength B according to the Boltzmann (thermal) distribution,

$$P = \frac{1 - \exp(-\mu B/kT)}{1 + \exp(-\mu B/kT)} \sim \mu B/2kT \qquad [4]$$

where k is the Boltzmann constant, and μ is the nuclear magnetic moment. For example, assuming T at room temperature (~296 K) and a field strength of 1.5 T, the proton spin polarization is $\approx$ 0.0005%. This value can be improved by increasing the magnetic field or lowering the temperature. However, given the large quantity of available protons found in most samples of biological interest (usually in the form of H_2O), NMR signal intensity is usually adequate at magnetic fields of ~1 T despite the low polarization. This is in contrast to the laser-polarization of noble gases (i.e., ^{129}Xe and ^{3}He), where polarizations of order ~1–50% can be achieved *independent* of magnetic field strength. This factor of 10^4 to 10^5 increase in polarization is balanced by the 1/3000 ratio of gas to liquid density [at standard temperature and pressure (STP)] and the lower gyromagnetic ratio of the spin-$\frac{1}{2}$ noble gases compared to that of ^{1}H [$\gamma(^3\text{He}):\gamma(^1\text{H}) = 0.76$; $\gamma(^{129}\text{Xe}):\gamma(^1\text{H}) = 0.28$]. Thus in high magnetic fields, one can expect comparable magnetization density, and hence NMR signals per unit volume, from protons (in liquid) and LP noble gases. At low fields (e.g., 20.6 G) LP noble gas imaging is still feasible, whereas proton imaging is impractical unless a large "prepolarizing" field is used to enhance the extremely low proton spin polarization (see Table 1).

A more quantitative discussion should begin with signal-to-noise considerations. By approximating the ensemble of polarized nuclear spins as a driven solenoid coupled to the pickup (or receiver) coils, Hoult and Richards deduce an expression for the detected NMR signal ξ_S (*15*):

$$\xi_S = (B_r/i_r)V_S\omega_0 M_0. \qquad [5]$$

Here, (B_r/i_r) is the magnetic field strength per unit current that the pickup coil can produce, V_S is the sample volume, ω_0 is the Larmor frequency, and M_0 is the sample magnetization given by the product of the polarization P, density of spins N_S, and the magnetic moment $\mu/2$:

$$M_0 = PN_S\mu/2. \qquad [6]$$

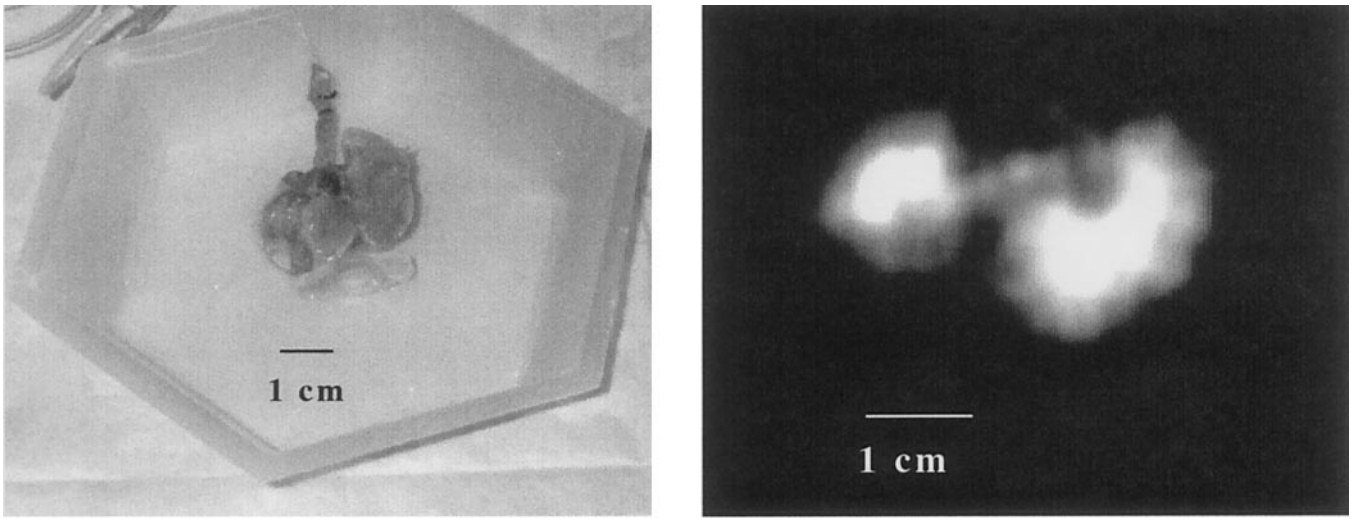

FIG. 6. Low field LP ^{3}He images of excised rat lungs. Excised rat lungs (a) were filled with LP ^{3}He gas and (b) imaged at 20.6 G.

Combining Eqs. [5] and [6], and noting that $\omega_0 = \gamma B$, one finds

$$\xi_S = (B_r/i_r)V_S\gamma BPN_S\mu/2. \qquad [7]$$

The dominant noise source for sufficiently small samples at high field, and practically any sample at low field, is Johnson noise from the pickup coils at temperature T

$$\xi_N = (4kTR\Delta f)^{1/2}, \qquad [8]$$

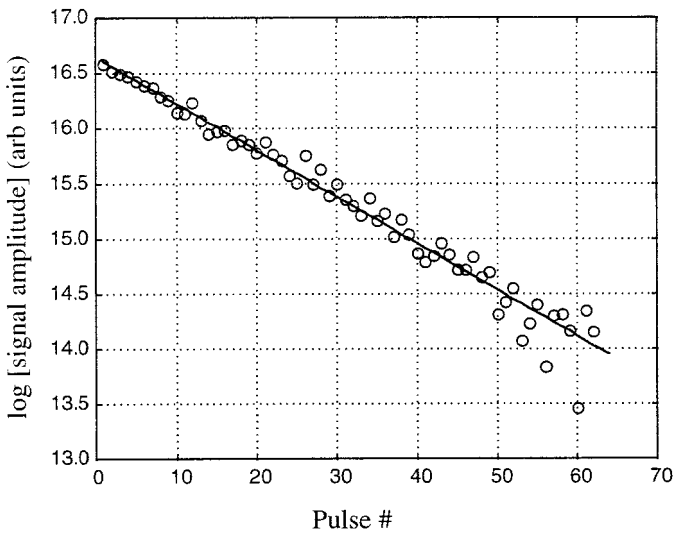

FIG. 7. Example T_1 data for LP ^{3}He inside excised rat lungs at 20.6 G. With the calibrated flip angle of 9.5° and T_R of 540 ms, the data shows a T_1 of 19 s for LP ^{3}He inside the lungs.

where R is the coil resistance and Δf is the noise bandwidth of the system. Inductively coupled noise from samples with weak electrical conductivity (e.g., biological tissue) scales linearly with the NMR frequency: $\xi_N \sim \omega \sim B$. This latter "tissue noise" dominates over coil Johnson noise only in large biological samples at high fields. [*Note:* due to the RF skin depth of the coil, there is also a weak dependence on NMR frequency, and hence magnetic field: $\xi_N \sim \omega^{1/4} \sim B^{1/4}$. For simplicity of discussion, we will ignore this weak effect here.]

Dividing Eq. [7] by Eq. [8], one obtains the familiar expression for the NMR signal-to-noise-ratio (SNR):

$$\mathrm{SNR} = \frac{(B_r/i_r)V_S\gamma BPN_S\mu/2}{\sqrt{4kTR\Delta f}}. \qquad [9]$$

Note that P in the equations above is linearly dependent on the applied magnetic field for thermally polarized samples: i.e., SNR $\sim B^2$. As mentioned earlier, a prepolarizing field B_P is sometimes applied that is purposefully stronger than the magnetic field B in which the nuclei precess (*16, 17*); in such cases, SNR is proportional to $B_P \times B$. In contrast, P is field independent for laser-polarized noble gases and hence SNR depends only linearly on B.

Assuming similar coil characteristics for detecting both thermally and laser-polarized samples, the ratio of SNRs scale as

$$\mathrm{SNR}(LP)/\mathrm{SNR}(thermal) \propto 1/B_P. \qquad [10]$$

Equation [10] gives the expected SNR from laser-polarized noble gases when compared with a thermally polarized sample at *the same field.* Furthermore, this equation can be directly

TABLE 1
Comparison of Thermally Polarized Water and Laser-Polarized ^{3}He and ^{129}Xe Magnetizations at High and Low Fields

	^{1}H (water)	^{3}He	^{129}Xe
Spin densities at STP (assuming pure samples)	6.7×10^{22} (^{1}H nuclei/cc)	2.7×10^{19} (^{3}He nuclei/cc)	2.7×10^{19} (^{129}Xe nuclei/cc)
Gyromagnetic ratio γ (10^8 rad/s/T)	2.67	2.04	0.74
High Field ($B_0 = 1.5$ T)			
Larmor frequency	63.8 MHz	48.6 MHz	17.6 MHz
polarization	5.1×10^{-6}	$(1–5) \times 10^{-1}$	$(1–10) \times 10^{-2}$
magnetization density (10^{18} μ_N/cc)	**0.96**	**5.7–29**	**0.2–2.1**
Low Field ($B_0 = 0.002$ T)			
frequency	87.9 kHz	67.0 kHz	24.5 kHz
polarization	7×10^{-9}	$(1–5) \times 10^{-1}$	$(1–10) \times 10^{-2}$
magnetization density (10^{18} μ_N/cc)	**0.0013**	**5.7–29**	**0.2–2.1**

applied at varying field strengths, which is not necessarily true of a comparison of SNR at high and low fields for LP or thermally polarized samples alone. In this latter case, establishing a clear field dependence is complicated by the fact that coil characteristics (i.e., B_r/i_r in Eq. [9]) can be quite varied in design and behavior over large frequency ranges. For instance, at low frequencies (kHz) one can utilize multiple turn coils to enhance signal detection, a technique not easily parameterized by the main applied field.

As an example, we compare $1/B_P$ at 1.5 T (a typical clinical imager field strength) and 20 G. If we assume SNR($LP\ gas$) $\sim$ 10 $\times$ SNR($water$) at high field, then at the lower field we expect SNR($LP\ gas$) $\sim$ 750 $\times$ 10 $\times$ SNR($water$). Thus the low field SNR of a LP noble gas sample exceeds the low field SNR of a thermally polarized water sample by nearly four orders of magnitude.

(ii) Reduced Effect of Magnetic Susceptibility Gradients at Low Fields

As noted above, one of the advantages of low field imaging is to reduce both imaging distortions and line broadening due to heterogeneous magnetic susceptibilities. Assuming that a given susceptibility χ is linear, we have the simple expression for the resultant magnetic field B'

$$B' = B_0(1 + \chi), \qquad [11]$$

where B_0 is the main applied field. When χ is nonuniform in a sample ($B' = B'(\boldsymbol{r})$), spins will precess at a frequency $\gamma(B'(\boldsymbol{r}) + \boldsymbol{G} \cdot \boldsymbol{r})$ in the presence of an imaging gradient $\boldsymbol{G}$. Thus the usual mapping of spin frequencies (with gradients on) to real space is no longer an accurate representation of the spatial distribution of spins, and will result in imaging distortions. Two possibilities to reduce or eliminate such artifacts is to either increase the imaging gradient strengths to a degree which makes the susceptibility-induced frequency shifts much smaller than the imaging gradient (i.e., $\boldsymbol{G} \cdot \boldsymbol{r} \gg$ variations in $B'(\boldsymbol{r})$), or to produce the same effect by decreasing the main field B_0. In our low field setup we use gradients $\frac{1}{10}$ the strength of high field (clinical) imaging gradients, but the drop of nearly three orders of magnitude in the main field B_0 implies a hundred-fold improvement in reducing artifacts arising from susceptibility heterogeneity.

In addition to distortions, variations in χ lead to spectral line broadening. For example, let χ be characterized by a Gaussian spatial distribution with mean χ_0 and standard deviation $\Delta\chi$. The susceptibility deviation $\Delta\chi$ causes decoherence for *stationary* nuclei precessing in the resultant varying fields. This decoherence is characterized as a contribution to T_2^* of the form

$$1/T_2^* = 1/T_2 + \gamma\Delta\chi B_0/2. \qquad [12]$$

For *diffusing* nuclei (with diffusion coefficient D), one must consider a random walk of the ensemble's phase, providing an additional contribution to T_2^*

$$1/T_{2diff}^* = [\gamma(\Delta\chi/l)\, B_0]^2 D\tau^2/3, \qquad [13]$$

where l is a characteristic length over which χ varies by $\Delta\chi$, and τ is related to the echo time used in the imaging sequence. Strictly speaking, this expression is relevant for diffusion through a steady gradient field. In practice, susceptibility-induced gradients can fluctuate, with an upper bound on phase shifts they induce. The result is a "restricted random walk" that can only be described by Eq. [13] in a "slow diffusion" regime where the characteristic diffusion time is large compared to the frequency shifts due to susceptibility heterogeneity, i.e., $(\gamma\Delta\chi B_0)\ (l^2/D) \gg 1$. In a "fast diffusion" regime, $(\gamma\Delta\chi B_0)\ (l^2/D) \ll 1$ and Eq. [13] is no longer valid; instead, the correct expression is of the form

$$1/T_{2diff}^* = (\gamma\Delta\chi B_0)^2 (l^2/D). \qquad [14]$$

Both Eqs. [13] and [14] depend on the main field B_0 squared, unlike Eq. [12] which is linear in B_0.

Clearly, at low fields there will be significantly less decoherence due to magnetic susceptibility gradients than at high fields, in addition to the reduction in imaging distortions. This has been demonstrated experimentally in a previous report (*10*) and will be particularly effective for low field noble gas NMR in heterogeneous samples such as the lung or reservoir rocks (*18*).

(iii) Imaging Resolution Considerations

An immediate benefit of the reduced magnetic susceptibility at low fields is the long T_2^* for heterogeneous samples. As mentioned earlier, T_2^* was measured to be greater than 100 ms for LP ^{3}He at STP when infused into a sample of excised rat lungs at 20.6 G; however, this value does not fully demonstrate the aforementioned B_0^2 improvement over high field because of both B_0 inhomogeneity and uncertainties due to the influence of radiation damping (discussed below). Thus one can expect even longer LP ^{3}He T_2^* at low fields with better magnetic field shimming and reduced radiation damping.

The positive effect of a longer T_2^* on imaging resolution (Δx) can be seen in the expression from Callaghan (*12*)

$$\Delta x(T_2^* - limited) = [(\gamma G/(2\pi)) \times \pi T_2^*]^{-1} = 2/(\gamma G T_2^*), \quad [15]$$

where γ is the gyromagnetic ratio in angular units and G is the applied gradient strength. Weak gradients are used at low fields to keep field variations across the sample small relative to the main magnetic field, and hence to validate the secular approximation used to generate undistorted images from MRI data (*19, 20*). Typically, 0.1 G/cm gradients were used in our low field setup. At high fields, gradients for human subjects are limited to ~1 G/cm by safety considerations. Assuming T_2^* is 100 and 5 ms at low and high fields, respectively, one obtains a corresponding $\Delta x(T_2^* - limited) = 0.1$ and 0.2 mm for LP ^{3}He. It is important to note that the high and low field T_2^* values used in this estimate were measured in "bulk" LP ^{3}He imbibed in the lungs; locally, T_2^* may differ in a given voxel. Nonetheless, assuming that these times are reasonable for an average voxel, the calculated values serve as a basis of comparison for low and high field noble gas MRI, and will be referred to as Δx_{opt}.

Next, consider the image resolution set by finite data acquisition time. At low fields we typically acquire NMR imaging data for 128 ms, corresponding to a frequency resolution of 1/(128 ms) = 7.8 Hz. For comparison, assume that we use the same acquisition time at high field and employ the same imaging gradient values as above (respectively). This frequency resolution then translates to an image resolution of 0.2 mm at low field, and 0.02 mm at high field. Clearly, given the quoted values for T_2^*, one could use a longer acquisition time at low fields, while a shorter acquisition time at high field would not degrade resolution.

The effect of diffusion for gases is quite significant. At STP, ^{3}He has a diffusion coefficient $D = 1.8 \times 10^{-4}$ m^2/s. A simple calculation gives the one-dimensional distance an ^{3}He atom will diffuse in a data acquisition time t_{aq} of 128 ms

$$\Delta x_{diff} = (2Dt_{aq})^{1/2} = 6.8 \text{ mm}. \quad [16]$$

As Callaghan notes (*12*), one should not consider Δx_{diff} as a strict limit on resolution; rather, it results in spectral broadening that, in the presence of imaging gradients, will degrade resolution in a manner weighted toward the T_2^*-limited value. Therefore, ignoring the small effects of a finite data acquisition time, we find the effective image resolution of LP ^{3}He gas in the lung at STP to be

$$\Delta x = 1.34[\Delta x_{diff} \Delta x_{opt}^2]^{1/3} = 0.6 \text{ mm for low fields} = 0.9 \text{ for high fields}. \quad [17]$$

This analysis shows that low and high field MRI of laser-polarized gas offer comparable resolution for human lung imaging (of course, sufficient NMR SNR is required to realize such resolution—see discussion above). The relatively weak gradients used at low fields are compensated by the intrinsically longer T_2^*. However, because of the high degree of diffusion, gas phase imaging at both high and low fields only allows for resolution just under 1 mm. For nonliving subjects, this resolution can be improved in principal by increasing the gas pressure; and, at high fields, by increasing the strength of the imaging gradients.

(iv) Reduced RF Shielding at Low Frequencies

Another advantage for low field imaging is that oscillating electromagnetic fields can penetrate much deeper into conducting materials at the low Larmor frequencies resulting from the reduction in field strength. The "skin depth" δ that characterizes the distance RF can propagate inside a conductor before it is attenuated by 63% ($1/e$) is given by (*21*)

$$\delta = \frac{1}{\sqrt{\pi f \sigma \mu}}, \quad [18]$$

where f is the Larmor frequency, σ is the conductivity of the conductor, and μ is the magnetic susceptibility of the conductor. For example, at 100 kHz, δ is 400 μm for brass and 200 μm for copper. On the other hand, δ is 13 μm and 7 μm for brass and copper, respectively, at 100 MHz. Thus the imaging of spaces surrounded by conductive materials, which is not feasible with high field NMR, may be achieved with low field

MRI of LP noble gas. This capability has also been demonstrated in the previous report (*10*).

(v) Radiation Damping

Radiation damping in NMR is well known (*22*, *23*) and is generally observed at high fields where liquid-phase magnetization due to thermal polarization is large, T_2^* is long, and pickup coil Q is very high. Briefly stated, radiation damping describes the effect of the "back reaction" field of the pickup coil on the sample magnetization. The precessing spins cause a current to flow in the pickup coil, which in turn produces a field that acts on the sample magnetization and brings it back into the longitudinal direction in the lower energy configuration (i.e., aligned with the main magnetic field). The characteristic time for this process is τ_{rd}

$$\tau_{rd} = (2\pi\eta\gamma Q|\mathbf{M}|)^{-1}, \qquad [19]$$

where η is the filling factor, and $\mathbf{M}$ is the magnetization vector. For LP gases, radiation damping is in stark contrast to T_1 and T_2^* processes, which act to *reduce* the magnitude of $\mathbf{M}$ (recall that T_1 relaxation restores the magnetization to thermal equilibrium, which is much smaller than the magnetization achieved with laser-polarization). In comparison, radiation damping does not affect the magnitude of $\mathbf{M}$, but its direction.

Because radiation damping is observed for large magnetizations, it is not surprising that we observed this effect at low fields in our LP ^{3}He samples. In fact, optically pumped ^{3}He Zeeman masers rely on radiation damping to sustain an active oscillation, as was first demonstrated at 32 G (*24*). A related device we have developed is a cohabitating, two-species ^{3}He/^{129}Xe Zeeman maser operating at fields ~1–3 G (*25*).

Due to long T_1 and nonrenewable polarization of the LP noble gases, one generally utilizes small flip angles to acquire NMR imaging data. If the flip angle α is held constant, the longitudinal LP noble gas magnetization $\mathbf{M}$ is depleted each pulse by a factor of (1-cos α) and by T_1 relaxation between pulses. Radiation damping acts to restore $\mathbf{M}$ back along the $\mathbf{B_z}$ axis, resulting in an effectively smaller flip angle α in the case where the interpulse spacing T_R is much less than T_1 and the noble gas is laser-polarized in the lower energy state. This radiation damping effect is clearly seen in Fig. 8, which shows flip angle calibration data taken with the pickup coils tuned both on and off resonance with the ^{3}He Larmor frequency (i.e., with a high and low pickup coil Q, respectively). Recall that our drive coils are independent from and orthogonal to our pickup coils; thus we can be confident that the same RF power over the same duration is delivered to the sample regardless of the pickup coil tuning. However, by changing the pickup coil tuning, the "back reaction" field generated while $\mathbf{M}$ has a transverse component precessing around $\mathbf{B_z}$ is also changed. As expected, the detuned case minimizes the effect of radiation damping, and the effective flip angle is greater.

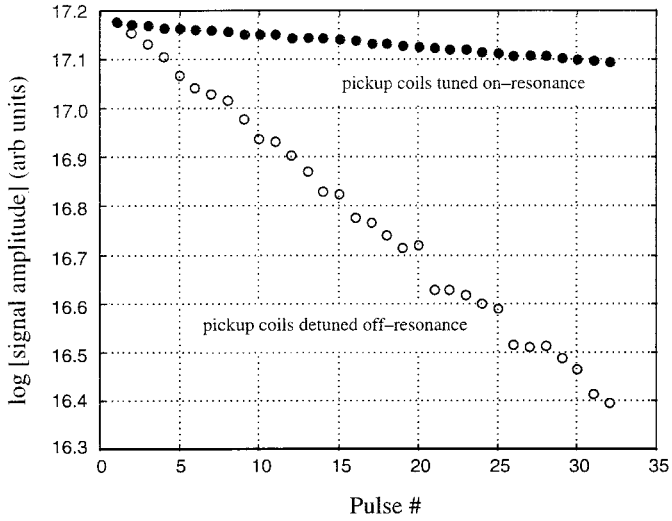

FIG. 8. The effect of coil tuning on LP ^{3}He flip angle measurements at 20.6 G in a sealed glass cell, demonstrating radiation damping in our low-field system. The (●) data were taken with pickup coils tuned on resonance with the ^{3}He Larmor frequency (67 kHz). With exactly the same RF pulse power and duration, a dramatically increased flip angle (○) was observed when the pickup coils are detuned far off-resonance (i.e., with a greatly reduced pickup coil Q). Fits to the (●) and (○) data yield apparent flip angles of 4.2° and 12.8°, respectively.

Another way to examine the situation is to vary the acquisition time between LP ^{3}He flip angle calibration data. The flip angle calibration sequence employs "crusher" gradients directly after each acquisition period to effectively remove any residual transverse magnetization. Consequently, one expects to see a larger effective flip angle when shorter acquisition times are chosen, because the crushers dephase any residual transverse magnetization that radiation damping could have restored to the longitudinal direction. Figure 9 shows three data sets supporting this expectation, with acquisition times of 1024, 256, and 64 ms. There is a clear trend of larger effective flip angles for shorter acquisition times.

Finally, Fig. 10 shows τ_{rd} measurements made from 64 successive FIDs from LP ^{3}He in excised rat lungs at 20.6 G. It is well known that FIDs follow a decay of the form $sech\,(t/\tau_{rd})$ when radiation damping dominates over the usual T_2^* exponential decay (i.e., $\tau_{rd} \ll T_2^*$). From Eq. [19], τ_{rd} depends on $|\mathbf{M}|$, which is decreasing after each FID acquisition due to magnetization dephased by the subsequent crusher gradients. Since τ_{rd} is inversely proportional to $|\mathbf{M}|$, one expects τ_{rd} to increase with each successive FID, which is observed in the data. (*Note:* based on Fig. 10, which shows τ_{rd} increasing from 50 to 120 ms, one can assume that $T_2^* > 100$ ms for ^{3}He imbibed into excised rat lungs at 20.6 G, as we stated earlier. Values of T_2^* greater than 100 ms have also been measured with the coils detuned off resonance.)

While these results are unsurprising, they do raise the question of how to quantify parameters of interest for low field noble gas NMR. For example, T_1 data shown in Fig. 7 for a

sample rat lung was taken with the pickup coils tuned on resonance. If the coils were tuned off resonance, both a larger apparent flip angle would have resulted, as well as a shorter apparent T_1. As for imaging, the previous discussion on resolution leads one to expect better resolution with decreasing magnetization (i.e., less radiation damping), since dephasing times will increase as **M** decreases. This is counterbalanced by the loss of SNR as **M** decreases, and the fact that radiation damping plays less of a role when imaging gradients are applied (this last effect enabled better than 1 mm^2 resolution in our low field LP ^{3}He imaging, despite large **M**).

CONCLUSION

Low field imaging of laser-polarized noble gas offers many advantages while retaining the resolution one expects from a high field system. Setting up a low field apparatus is straightforward and inexpensive, utilizing easy-to-manufacture equipment and off-the-shelf electronic components of modest cost. Furthermore, a low field MRI system is robust and portable and does not require specialized accommodations (e.g., a shielded room or cryogenic cooling for the magnet). Operating at low fields (<100 G) results in low Larmor frequencies (kHz), which reduces both RF power requirements and simplifies the electronics required. Also, these low frequencies have longer RF skin depths, thus allowing gas-space imaging inside conductive materials. At low magnetic fields there is a reduced effect of magnetic susceptibility heterogeneity, resulting in longer T_2^* and improved noble gas image resolution and distortion reduction. This reduced susceptibility effect is also relevant to restricted gas diffusion experiments conducted in porous media, where sample heterogeneity limits the technique's effectiveness at high fields (*4*). Finally, the long T_2^* at low fields and the high spin polarization in LP ^{3}He make radiation damping effects observable (e.g., during low flip angle calibrations), which must be taken into account when interpreting LP noble gas NMR data.

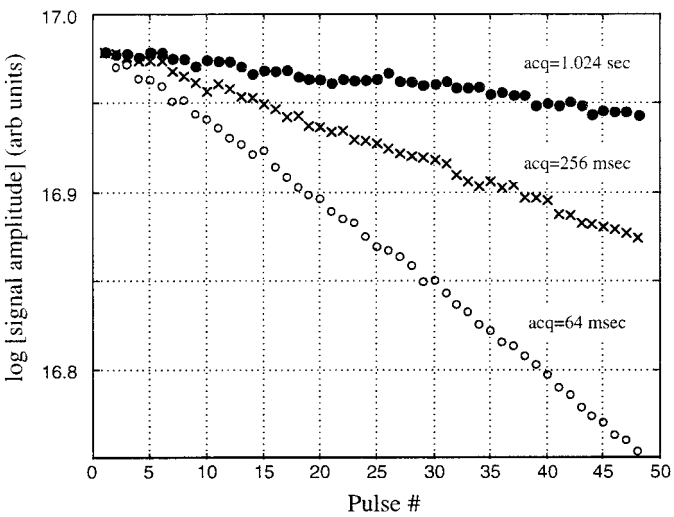

FIG. 9. The effect of data acquisition time on LP ^{3}He flip angle measurements in a sealed glass cell, demonstrating the effect of radiation damping in our low-field system. All data were taken at 20.6 G with the pickup coils tuned on-resonance with the ^{3}He Larmor frequency (67 kHz), and with exactly the same power and duration RF pulse. The upper data (●) had an FID acquisition time (acq) of 1.024 s; the middle data (×) had acq = 256 ms; and the lower data (○) had acq = 64 ms. Apparent flip angles are 2.4°, 3.9°, and 5.6°, respectively.

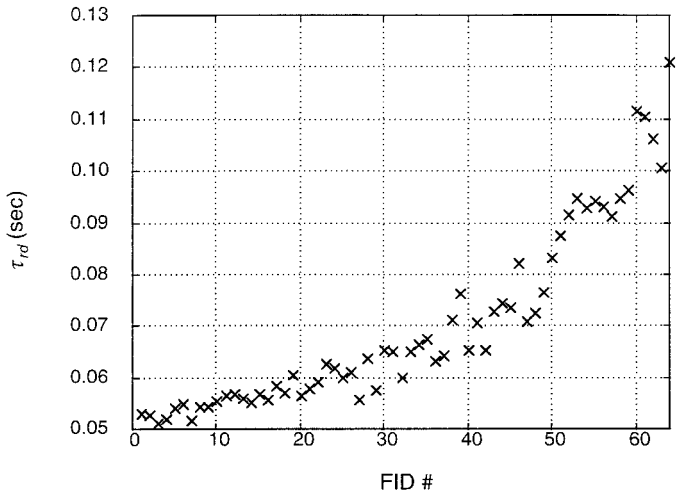

FIG. 10. Measurements of radiation damping time (τ_{rd}) for LP ^{3}He inside excised rat lungs at 20.6 G. Fits to $sech(t/\tau_{rd})$ are shown for each of the FIDs acquired from sequential low flip angle pulses. With each successive FID, the ^{3}He magnetization is reduced, hence radiation damping is lessened (i.e., τ_{rd} increased).

ACKNOWLEDGMENTS

We gratefully acknowledge J. Moore for preparation of excised rat lungs. This work was supported by NSF Grant BES-9612237, NASA Grants NAGW-5025 and NAG5-4920, the Whitaker Foundation, and the Smithsonian Institution. G.P.W. gratefully acknowledges support from an NSF Graduate Research Fellowship.

REFERENCES

1. M. S. Albert, G. D. Cates, B. Driehuys, W. Happer, B. Saam, C. S. Springer Jr., and A. Wishnia, Biological magnetic resonance imaging using laser-polarized ^{129}Xe, *Nature* **370,** 199–201 (1994).
2. For a review, see H.-U. Kauczor, R. Surkau, and T. Roberts, *Eur. Radiol.* **8,** 820–827 (1998) and references therein.
3. Y.-Q. Song, H. C. Gaege, T. Pietrass, G. A. Barrall, G. C. Chingas, M. R. Ayers, and A. Pines, Spin-polarized ^{129}Xe gas imaging of materials, *J. Magn. Res. A* **115,** 127–130 (1995).
4. R. W. Mair, D. G. Cory, S. Peled, C-H. Tseng, S. Patz, and R. L. Walsworth, Pulsed-field-gradient measurements of time-dependent gas diffusion, *J. Magn. Reson.* **135,** 478–486 (1998).
5. T. G. Walker and W. Happer, Spin-exchange optical pumping of noble-gas nuclei, *Rev. Mod. Phys.* **69,** 629–642 (1997).
6. G. Eckert, W. Heil, M. Meyerhoff, E. W. Otten, R. Surkau, M. Werner, M. Leduc, P. J. Nacher, and L. D. Schearer, A dense

polarized ^{3}He target based on compression of optically pumped gas, *Nucl. Instr. Methods Phys. Res. A* **320,** 53–65 (1992).

7. L. Darrasse, G. Guillot, P.-J. Nacher, and G. Tastevin, *in* "Proc. Intl. Soc. Magn. Reson. Med. 6th Meeting," p. 449 (1998).
8. B. Saam, N. Drukker, and W. Happer, Edge enhancement observed with hyperpolarized ^{3}He, *Chem. Phys. Lett.* **263,** 481–487 (1996).
9. M. P. Augustine, A. Wong-Foy, J. L. Yarger, M. Tomaselli, A. Pines, D. M. Ton That, and J. Clarke, Low field magnetic resonance images of polarized noble gases obtained with a dc superconducting quantum interference device, *Appl. Phys. Lett.* **72,** 1908–1910 (1998).
10. C. H. Tseng, G. P. Wong, V. R. Pomeroy, R. W. Mair, D. P. Hinton, D. Hoffmann, R. E. Stoner, F. W. Hersman, D. G. Cory, and R. L. Walsworth, Low-field MRI of laser polarized noble gas, *Phys. Rev. Lett.* **81,** 3785–3788 (1998).
11. R. J. Hanson and F. M. Pipkin, Magnetically shielded solenoid with field of high homogeneity, *Rev. Sci. Inst.* **36,** 179–188 (1965).
12. P. T. Callaghan, "Principles of Nuclear Magnetic Resonance Microscopy," Oxford University Press, Oxford (1991).
13. P. Bachert, L. R. Schad, M. Bock, M. V. Knopp, M. Ebert, T. Großman, W. Heil, D. Hofmann, R. Surkau, and E. W. Otten, Nuclear magnetic resonance imaging of airways in humans with use of hyperpolarized ^{3}He, *Magn. Reson. Med.* **36,** 192–196 (1996).
14. X. J. Chen, M. S. Chawla, G. P. Cofer, L. W. Hedlund, H. E. Möller, and G. A. Johnson, Hyperpolarized ^{3}He NMR lineshape measurements in live guinea pig lung, *Magn. Reson. Med.* **40,** 61–64 (1998).
15. D. I. Hoult and R. E. Richards, The signal-to-noise ratio of the nuclear magnetic resonance experiment, *J. Magn. Reson.* **24,** 71–85 (1976).
16. P. T. Callaghan, C. D. Eccles, and J. D. Seymour, An earth's field nuclear magnetic resonance apparatus suitable for pulsed gradient spin echo measurements of self-diffusion under Antarctic conditions, *Rev. Sci. Instr.* **68,** 4263–4270 (1997).
17. A. Mohoric, J. Stepisnik, M. Kos, and G. Planinsic, Self-diffusion imaging by spin echo in Earth's magnetic field, *J. Magn. Reson.* **136,** 22–26 (1999).
18. R. A. Waggoner and E. Fukushima, Velocity distribution of slow fluid flows in Bentheimer sandstone: An NMRI and propagator study, *Magn. Reson. Imaging.* **14,** 1085–1091 (1996).
19. J. M. Blackledge, "Quantitative Coherent Imaging," Academic Press, London (1989).
20. P. T. Callaghan and C. D. Eccles, Diffusion-limited resolution in nuclear magnetic resonance microscopy, *J. Magn. Reson.* **78,** 1–8 (1988).
21. D. J. Griffiths, "Introduction to Electrodynamics," 2nd ed., Prentice Hall, New Jersey (1989).
22. N. Bloembergen and R. V. Pound, Radiation damping in magnetic resonance experiments, *Phys. Rev.* **95,** 8–12 (1954).
23. A. Abragam, "The Principles of Nuclear Magnetism," Clarendon Press, Oxford (1961).
24. H. G. Robinson and Than Myint, ^{3}He nuclear zeeman maser, *Appl. Phys. Lett.* **5,** 116–118 (1964).
25. R. E. Stoner, M. A. Rosenberry, J. T. Wright, T. E. Chupp, E. R. Oteiza, and R. L. Walsworth, Demonstration of a two species noble gas maser, *Phys. Rev. Lett.* **77,** 3971–3974 (1996).